MULTI-SOURCE QUANTITATIVE PHOTOACOUSTIC TOMOGRAPHY WITH DETECTOR RESPONSE FUNCTION AND LIMITED-VIEW SCANNING*

Jing Feng

School of Biomedical Engineering, Shanghai Jiao Tong University, Shanghai, China

Weifeng Zhou

School of Mathematics and Physics, Qingdao University of Science and Technology, Qingdao, Shandong, China

Hao Gao

Department of Mathematics and School of Biomedical Engineering, Shanghai Jiao Tong University, Shanghai, China
Email: hao.gao.2012@gmail.com

Abstract

A practical image reconstruction method for multi-source quantitative photoacoustic tomography (QPAT) is proposed in this work with the consideration of detector response function and limited-view scanning. First, the correct detector response function, i.e., spatial impulse response (SIR) and acousto-electric impulse response (EIR), is considered for the ultrasonic transducer to accurately model the acoustic measurement; second, acoustic data is only measured near optical sources with meaningful signal-to-noise ratio (SNR), i.e., the limited-view scanning, which also reduces the data acquisition time for point transducer. However, due to the incomplete limited-view data, a two-step image reconstruction method (i.e., to first reconstruct initial acoustic pressure and then reconstruct optical coefficients) no longer applies, since it is neither possible nor necessary to robustly reconstruct initial acoustic pressure with limited-view data. Therefore, here we propose a direct image reconstruction method that incorporates SIR, EIR and limited-view scanning in a coupled opto-acoustic forward model, regularizes the nonlinear QPAT data fidelity with tensor framelet sparsity, and then solves the QPAT problem with Quasi-Newton method based alternating direction method of multipliers.

Mathematics subject classification: 65N06, 65B99.
Key words: Quantitative photoacoustic tomography, Alternating direction method of multipliers, Image reconstruction.

1. Introduction

Photoacoustic tomography (PAT) (see e.g., [7, 14, 24, 27, 33]) is developed in recent years for non-invasively imaging soft biological tissues with various biomedical applications. On one hand acoustic imaging allows higher spatial resolution than optical imaging owing to the weaker acoustic scattering than optical scattering; on the other hand optical contrasts are higher and richer than acoustic contrasts. In this sense, PAT synergizes the conventional optical and acoustic imaging with the ability of imaging high and rich optical contrasts in high resolution. However, it is still unclear whether PAT can reveal optical contrasts in depth

with high resolution, which is the goal of quantitative PAT (QPAT), e.g., the review paper [12] and the references therein.

There are two inverse problems in QPAT: acoustic inverse problem and optical inverse problem. Specifically, the acoustic inverse problem is to estimate the initial acoustic pressure from boundary acoustic measurement [35]; the optical inverse problem is to reconstruct the optical contrasts from initial acoustic pressure [12]. The simultaneous reconstruction of more than one optical coefficients is not unique with only single optical illumination or optical wavelength. Therefore QPAT with multiple optical wavelengths [10, 12, 25, 28], multi-source illuminations (MS-QPAT) (e.g., [5, 17, 19, 29, 31, 32, 37, 43], or their combination [6] have been investigated so that all optical coefficients can be uniquely reconstructed. This work focuses on MS-QPAT.

In the conventional MS-QPAT, a full-rotation boundary acoustic data needs to be acquired following each optical illumination, which may result in different level of signal-to-noise (SNR) ratio, e.g, high SNR at the boundary close to optical sources. Consequently these low-SNR data may degrade reconstructed image quality. To achieve a high SNR uniformly in the acquired data, the limited-view MS-QPAT is proposed [43], i.e., a partial-view boundary acoustic measurement following each optical illumination. In this way, high SNR can be uniformly maintained. Moreover, it can significantly reduce the scanning time proportional to scanning angles for point ultrasonic transducer. However, in addition to the SNR uniformity, for accurate QPAT reconstruction in practice, the detector response of acoustic transducer must be taken into account. Without considering detector response function, the reconstructed image quality can be degraded with distortion and reduced spatial resolution [4].

In this paper, for the practical QPAT image reconstruction, we consider MS-QPAT with limited-view scanning and detector response function. Due to limited-view scanning, the aforementioned two-step approach for QPAT fails, since the acoustic reconstruction for initial acoustic pressure is unstable [36]. On the other hand, the reconstruction of initial acoustic pressure is not the ultimate goal, and thus it is not essential as long as optical contrasts can be reconstructed. Thus, we consider the direct reconstruction of optical contrasts from the acoustic measurement based on a coupled opto-acoustic forward model with SIR and EIR.

The paper is organized as follows: The proposed practical MS-QPAT forward model and the corresponding discretization are introduced in Section 2; the numerical method for solving the proposed MS-QPAT in nonlinear least squares will be developed in Section 3; the sparsity-regularized method with simple bound constraints for QPAT is investigated in Section 4; the proposed method is validated through numerical experiments in Section 5; finally, we will conclude in Section 6.

2. Practical QPAT

2.1. Coupled Opto-Acoustic Forward Model

The photoacoustic effect is fundamental to photoacoustic imaging. When the molecules within the soft tissues are exposed to short-pulse radiation (e.g., electromagnetic energy), the initial acoustic pressure $p_0(\vec{x})$ is excited because of the thermo-elastic mechanism, then the pressure wavefield $p(\vec{x}, t)$ propagates in tissues and is detected by the transducers that locate on a measurement aperture Ω_0 on the object boundary. This process can be separately modeled, i.e., as optical model and acoustic model.

The optical propagation in the biological tissues can be accurately described by radiative transfer equation (RTE), e.g., [16, 20–22] and the references therein. Here we consider the

following approximation of RTE, i.e., so-called diffusion approximation (DA)

$$-\nabla \cdot (D(\vec{x})\nabla\phi(\vec{x})) + \mu_a(\vec{x})\phi(\vec{x}) = 0, \quad \vec{x} \in \Omega_0, \tag{2.1a}$$

$$2\kappa D(\vec{x})(\vec{n} \cdot \nabla\phi(\vec{x})) + \phi(\vec{x}) = q(\vec{x}), \quad \vec{x} \in \partial\Omega_0. \tag{2.1b}$$

Robin boundary condition is assumed in the above equation, where $\phi(\vec{x})$ denotes optical density function, μ_a and μ_s denote the absorption and scattering coefficient respectively. Diffusion coefficient $D = 1/(3(\mu_a+\mu_s'))$, where $\mu_s' = (1-g)\mu_s$ is the so-called reduced scattering coefficient with g as the anisotropic scattering factor. Boundary coupling constant κ is used to account for the boundary refraction index mismatch [2].

When the tissue absorbs the radiation energy, the initial acoustic pressure

$$p_0(\vec{x}) = \Gamma(\vec{x})A(\vec{x}) \tag{2.2}$$

is excited [4], and when the stress and thermal confinements for PAT are satisfied, the acoustic pressure which generated by laser pulse illumination $I(t)$ propagates in the following equation [40]

$$\left(\nabla^2 - \frac{1}{c^2}\frac{\partial^2}{\partial t^2}\right)p(\vec{x},t) = -\frac{\beta}{C_p}A(\vec{x})\frac{\partial I(t)}{\partial t}, \tag{2.3}$$

where c, C_p and β denote the acoustic speed, specific heat capacity and isobaric volume expansion coefficient respectively. In (2.2), Γ is the given Grüneisen coefficient and $A(\vec{x}) = \mu_a(\vec{x})\phi(\vec{x})$ denotes the absorbed energy density. The pressure wavefield $p(\vec{x},t)$ measured by an ideal point transducer at location x_0 can be expressed as a solution to (2.3) as

$$p(\vec{x_0},t) = \frac{\beta}{4\pi C_p}\int_v d\vec{x}A(\vec{x})\frac{d}{dt}\frac{\delta(t - \frac{|\vec{x_0}-\vec{x}|}{c})}{|\vec{x_0} - \vec{x}|}. \tag{2.4}$$

Here, v denotes the support volume of the object and the integral denotes a hyperplane integral.

The inverse problem in QPAT is to reconstruct $(\mu_a(\vec{x}), D(\vec{x}))$. It is usually assumed that the absorbed energy density $A(\vec{x})$ or initial acoustic pressure $p_0(\vec{x})$ is known or can be first reconstructed from the boundary acoustic measurements $p(\vec{x},t)$ and then $\mu_a(\vec{x})$ and $D(\vec{x})$ are reconstructed by solving the corresponding light propagation RTE or DA approximation equation. However, initial acoustic signal $p_0(\vec{x})$ can not be stably reconstructed in limited-view QPAT owing to the incomplete acoustic measurements $p(\vec{x},t)$. Therefore, we need to reconstruct (μ_a, D) from $p(\vec{x},t)$ directly instead of reconstructing $A(\vec{x})$ or $p_0(\vec{x})$ first, i.e., we need to consider the following coupled opto-acoustic model

$$-\nabla \cdot (D(\vec{x})\nabla\phi(\vec{x})) + \mu_a(\vec{x})\phi(\vec{x}) = 0, \quad \vec{x} \in \Omega_0, \tag{2.5a}$$

$$2\kappa D(\vec{x})(\vec{n} \cdot \nabla\phi(\vec{x})) + \phi(\vec{x}) = q(\vec{x}), \quad \vec{x} \in \partial\Omega_0, \tag{2.5b}$$

$$p(\vec{x_0},t) = \int_v d\vec{x}A(\vec{x})H^A, \tag{2.5c}$$

with

$$H^A = \frac{\beta}{4\pi C_p}\frac{d}{dt}\frac{\delta(t - \frac{|\vec{x_0}-\vec{x}|}{c})}{|\vec{x_0} - \vec{x}|}. \tag{2.6}$$

2.2. Detector Response Function

Spatial impulse response (SIR) indicates the angular sensitivity of ultrasound transducer caused by its aperture averaging effect. SIR can cause a temporal distortion and extension
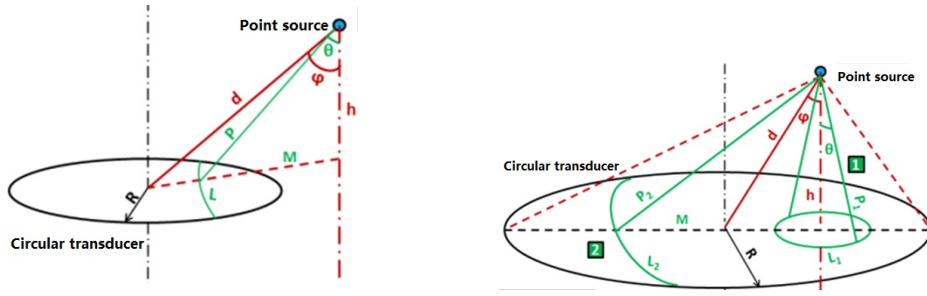
Fig. 2.1. Two transducer positions cases relative to point acoustic source

during the PA wave acquisition, which might lead to a blurring and degrade the image quality. Electro-acousto impulse response, an intrinsic property of transducer, indicates the frequency characteristic, e.g. central frequency and bandwidth. EIR is closely relevant to spatial resolution of ultrasound imaging and usually obtained by experimental measurement [3]. In practice, the aperture size of ultrasound transducer is finite, which causes a temporal distortion and extension of receiving acoustic signal on the transducer surface. In other words, each transducer element detects the source acoustic signal at different timestamps, and then those temporal profiles are superposed together, which lead to an averaging effect, i.e., angular sensitivity.

$$\widetilde{p}(\vec{x_0}, t) = \iint_{x \in S_d} p(\vec{x_d}, t) dS_d, \tag{2.7}$$

where $\vec{x_0}$, $\vec{x_d}$ and S_d denote the central location, the locations of the dth transducer position, and the surface area of transducer. (2.7) can be rewritten as a temporal convolution between $p(\vec{x_d}, t)$ and SIR is denoted by H^{SIR} [41].

For circular planar transducer, we can derive a temporal window function h_{TW} to simulate the aperture averaging and extension effect [41].

$$h_{TW}(t) = \sqrt{\tau_\theta^2 - t^2} \cdot \prod(\tau_\theta, t), \tag{2.8}$$

where τ_θ indicates the arrival time difference between the nearest element and the farthest element for a point pulse source, which can be written as

$$\tau_\theta = \begin{cases} \frac{2dR_T \cos\theta}{c_s} \cdot \dfrac{1}{\sqrt{d^2 + R_T^2 + 2dR_T \cos\theta} + \sqrt{d^2 + R_T^2 - 2dR_T \cos\theta}}, & R_T \leq d\cos\theta, \\[2mm] \dfrac{\sqrt{(2d\cos\theta + R_T)^2 + d^2\sin^2\theta} - d\sin\theta}{2c_s}, & R_T > d\cos\theta, \end{cases} \tag{2.9}$$

$$\prod(\tau_\theta, t) = \begin{cases} 1, & -\tau_\theta \leq t \leq \tau_\theta, \\ 0, & \text{else}, \end{cases} \tag{2.10}$$

where θ is the axis angle, R_T the radius of transducer surface, and d the distance between transducer and acoustic source respectively. Fig. 2.1 shows two transducer positions relative to point acoustic source. Fig. 2.2 gives the analytical solution and temporal window numerical solution of SIR with $R_T = 3mm$, $d = 10.77mm$ and $\theta = 8.13º$.
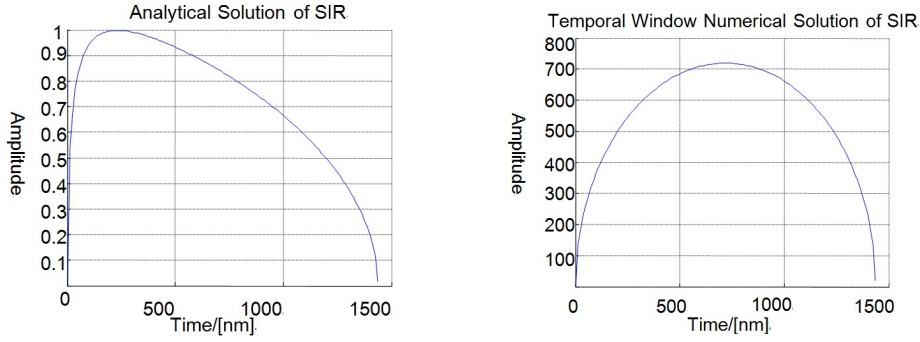
(a) SIR simulated by Dream Toolbox

(b) Temporal window solution

Fig. 2.2. Analytical solution and numerical solution of SIR

Besides, the measurement data for PAT is also related with the intrinsic characteristic of transducer. For instance, the central frequency and bandwidth determine the axial and lateral resolution of PAT respectively [4]. The transfer function of transducer is defined as EIR, which is equivalent to a band-pass filter [42]. EIR is determined by transducer's physical structure and obtained through experimental measurement denoted by H^{EIR} (Fig. 2.3).
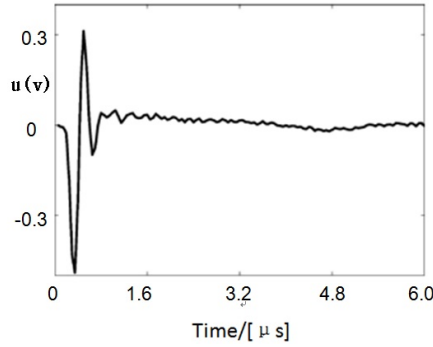

Fig. 2.3. EIR of ultrasound transducer

The acoustic model H of PAT can be obtained by convolving H^{A}, H^{SIR} and H^{EIR}, i.e.,

$$H = H^{\text{A}} * H^{\text{SIR}} * H^{\text{EIR}}. \tag{2.11}$$

Here $*$ denotes the temporal convolution. Note that this equation is still valid in the three-dimensional optoacoustic tomography [11].

2.3. Discretization

Here we consider the discretization of the aforementioned opto-acoustic model with detector response function.

2.3.1. Optical discretization

Using finite element method (FEM) method [2], the DA equation (2.1a) can be discretized by a triangular mesh. The unstructured meshing for discretizing the acoustic model is shown in Fig. 2.4 (left figure) and the linear interpolated for the Cartesian grid also can be seen here. Fig. 2.4 (right figure) also gives the triangular meshing for reconstruction.
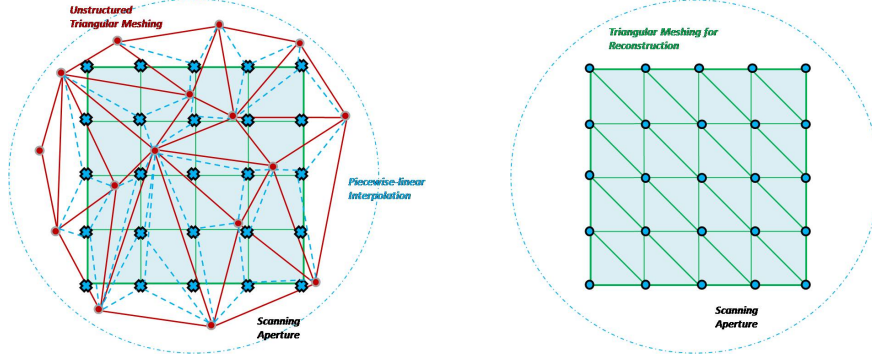

Fig. 2.4. FEM triangular meshing

Both optical density ϕ and optical coefficients (μ_a, D) can be discretized in piecewise constants using this kind of triangular mesh, and then the absorbed energy density $A(\vec{x})$ or $p_0(\vec{x})$ on the Cartesian grid of Ω can be linearly interpolated. The details of the corresponding discretization scheme are given in the following or readers can refer to [19, 43].

The photon density ϕ can be represented as

$$\phi(\vec{x}) = \sum_{i=1}^{N_p} \phi_i \varphi_i(\vec{x}), \quad [\Phi]_i = \phi_i \tag{2.12}$$

in the piecewise-linear bases $\{\varphi_i(\vec{x}_j) = \delta_{ij}, i, j \leq N_p\}$, and the optical coefficients (μ_a, D) can be discretized as

$$\mu_a(\vec{x}) = \sum_{k=1}^{N_t} \mu_k \chi_k(\vec{x}), \quad [U']_k = \mu_k, \tag{2.13}$$

$$D(\vec{x}) = \sum_{k=1}^{N_t} D_k \chi_k(\vec{x}), \quad [D']_k = D_k, \tag{2.14}$$

where $\{\chi_k = 1_{t_k}, k \leq N_t\}$ denote the piecewise-constant bases and N_p and N_t respectively denote the number of nodes and triangles of Ω_0 in Fig. 2.4.

Based on FEM [1], DA equation (2.1a) can be represented as the linear system

$$F\Phi = Q, \tag{2.15}$$

where

$$[F]_{ij} = \Sigma_{k=1}^{N_t} D_k \int_{t_k} \nabla\varphi_i \cdot \nabla\varphi_j d\vec{x} + \Sigma_{k=1}^{N_t} \mu_k \int_{t_k} \varphi_i \varphi_j d\vec{x} + \frac{1}{2\kappa} \int_\Gamma \varphi_i \varphi_j d\vec{x}, \tag{2.16}$$

$$[Q]_j = \frac{1}{2\kappa} \int_\Gamma q\varphi_j d\vec{x}. \tag{2.17}$$

2.3.2. Acoustic discretization

A finite-dimensional linear approximation of $A(\vec{x})$ is given by the following form

$$A(\vec{x}) = \sum_{n=0}^{N-1} A_n \theta_n(\vec{x}), \qquad (2.18)$$

with

$$\theta_n(\vec{x}) = \begin{cases} 1, & \text{if } |\vec{x} - \vec{x_n}| \leq \varepsilon, \\ 0, & \text{else}, \end{cases} \qquad (2.19)$$

where A_n denotes the absorbed energy density at $\vec{x}_n$ and $\theta_n(\vec{x})$ represents the uniform spherical expansion function for $A(\vec{x})$. Furthermore, (2.4) can be rewritten as the following matrix multiplication [11]

$$p(\vec{x}, t) = HA_n(\vec{x}). \qquad (2.20)$$

Here H denotes the acoustic system matrix. If the detector is ideal point-like, then $H = H^{\mathrm{A}}$ with

$$H^{\mathrm{A}} = \begin{cases} \dfrac{\beta c^2}{2C_p R_{q,n}}(R_{q,n} - c(n_t \cdot \triangle t)), & \text{for } \dfrac{R_{q,n} - \varepsilon}{c \cdot \triangle t} \leq n_t \leq \dfrac{R_{q,n} + \varepsilon}{c \cdot \triangle t}, \\ 0, & \text{else} \end{cases} \qquad (2.21)$$

Here $R_{q,n} = |\vec{x}_{d,q} - \vec{x}_n|$. $\vec{x}_q$ and $\vec{x}_n$ respectively denote the locations of qth transducer position and n^{th} source node in imaging region. If the transducer is finite-dimension, then $H = H^{\mathrm{A}} * H^{\mathrm{SIR}} * H^{\mathrm{EIR}}$.

The finite-dimensional discrete approximation of the SIR can be represented as

$$H^{\mathrm{SIR}}(\vec{x}_{d,q}, \vec{x}, t) = \sum_{n=0}^{N-1} H_n^{\mathrm{SIR}}(\vec{x}_{d,q}, t)\theta_n(\vec{x}). \qquad (2.22)$$

Then the linear operator H (2.11) can be discretized as a system matrix for acoustic modeling, which is also denoted as H here. Then the acoustic forward model based on SIR and EIR can be written as

$$p = Hp_0. \qquad (2.23)$$

Since the initial acoustic pressure p_0 on Ω can be obtained by the product of U and the photon density Φ which is interpolated from the triangular mesh on Ω_0 to the Cartesian grid on Ω, i.e.,

$$p_0 = (I_{\Omega_0 \to \Omega}\Phi) \cdot U, \qquad (2.24)$$

then the discretization of the coupled photoacoustic forward model can be summarized as

$$p(U, D) = H(I\Phi(U, D) \cdot U), \qquad (2.25)$$

where Φ is computed from DA Eq. (2.15).

2.4. Limited-View MS-QPAT

In the traditional MS-QPAT circumstance, 360° acoustic data are collected for each optical illumination. Therefore, those data collected far from optical excitation sources may have low SNR, and 360° rotations follow every optical excitation result in a long scanning time

with multiple rotations. To address this issue, we adopt limited-view scanning: the ultrasonic transducers are considered to rotate some degrees together with the illumination sources so that the acoustic data are collected only near the illumination sources with improved SNR and reduced scanning time, e.g., 90-degree data per illumination for four-source QPAT which is scanned in one rotation.

Suppose there are N_s optical illuminations in MS-QPAT and the acoustic data are detected in the full view, the boundary measurement can be written as the following equation

$$p_j^i = M_j^T[H(I\Phi^i(U, D) \cdot U)], \quad j \leq N_d, i \leq N_s, \tag{2.26}$$

where N_d is the numbers of the measurements and M_j denotes the measurement matrix corresponding to a specific time at detector position j.

However, in the limited-view MS-QPAT, the acoustic data are detected at the partial boundary of Ω, so the data acquisition index can be regarded as a subset of all the detector positions. Then the limited-view MS-QPAT can be written as the following

$$p_j^i = M_j^T[H(I\Phi^i(U, D) \cdot U)], \quad j \in \mathcal{J}_i, i \leq N_s, \tag{2.27}$$

where $\mathcal{J}_i$ denotes an index subset of $\{j = 1, \cdots, N_d\}$.

3. Image Reconstruction

3.1. Functional Gradient

Let Y denote the given limited-view acoustic data and $X = (U, D)$ denote the absorption and diffusion distribution, then using nonlinear least squares, the MS-QPAT image reconstruction can be modeled as

$$X = \arg\min_X \frac{1}{2}||p(X) - Y||^2. \tag{3.1}$$

Let $E(X) = \frac{1}{2}||p(X) - Y||^2$. Then based on the discrete forward model (2.27), we have

$$\sum_{i=1}^{N_s} \sum_{j \in \mathcal{J}_i} E_{ij}^2 = \frac{1}{2} \sum_{i=1}^{N_s} \sum_{j \in \mathcal{J}_i} \left(M_j^T H(I\Phi^i(U, D) \cdot U) - Y_{ij}\right)^2, \tag{3.2}$$

where $\mathcal{J}_i$ is the partial-view set of the detector positions during the ith optical illumination.

Define the adjoint acoustic problem

$$\Psi_a^i = H^T Q_a^i \tag{3.3}$$

with $Q_a^i = \sum_{j \in \mathcal{J}_i} E_{ij} M_j$, and define the adjoint optical problem

$$F^T \Psi_0^i = Q_0^i \tag{3.4}$$

with the adjoint optical source $Q_0^i = I^T(\Psi_0^i \cdot U)$. Then the numerical gradient of $E(X)$ can be represented as

$$\frac{\partial E}{\partial X_k} = \sum_{i=1}^{N_s} \Psi_0^{i\,T} \left(-\frac{\partial F}{\partial X_k}\right) \Phi^i + \Psi_a^{i\,T}\left[(I\Phi^i) \cdot \frac{\partial U}{\partial X_k}\right], \tag{3.5}$$

where X_k denotes to the kth element of (U, D). More details about the solution of the gradient are available in [43].

3.2. Quasi-Newton Method

Let $r = X - X_k$. Denote $E_k = E(X_k)$ and $\partial E_k = \frac{\partial E}{\partial X}|_{X=X_k}$. The quadratic Taylor expansion of $E(X)$ (3.1) is

$$Q_k(r) = E_k + \partial E_k^T r + \frac{1}{2} r^T H_k r, \tag{3.6}$$

where H_k denotes the Hessian matrix at X_k. Then the Newton direction r_k can be obtained

$$r_k = -H_k^{-1} \partial E_k. \tag{3.7}$$

Finally, the Newton iteration form for problem (3.1) can be written as

$$X_{k+1} = X_k + \lambda_k r_k. \tag{3.8}$$

Here λ_k denotes the iteration step length.

In order to avoid the computation of the second derivative in Hessian matrix, Quasi-Newton Method based on first-order derivative (i.e., the functional gradient) can be used to solve the problem (3.1) instead of Newton Method, for which BFGS is a popular scheme.

Let $s_k = X_{k+1} - X_k$ and $y_k = \partial E_{k+1} - \partial E_k$. Then the corresponding BFGS scheme is as follow

$$H_{k+1}^{-1} = V_k^T H_k^{-1} V_k + \rho_k s_k s_k^T \tag{3.9}$$

Here $\rho_k = \frac{1}{y_k^T s_k}$ and $V_k = I - \rho_k y_k s_k^T$.

However, H_k^{-1} in BFGS scheme is usually dense so that it may be prohibitive with respect to both computational speed and memory . Therefore, the following limited-memory BFGS (L-BFGS) [9, 26] is adopted

$$H_k^{-1}|_{L-BFGS} = (V_{k-1}^T \ldots V_{k-m}^T) H_{k,0}^{-1} (V_{k-m} \ldots V_{k-1})$$

$$+ \rho_{k-m} (V_{k-1}^T \ldots V_{k-m+1}^T) s_{k-m} s_{k-m}^T (V_{k-m+1} \ldots V_{k-1})$$

$$+ \cdots + \rho_{k-1} s_{k-1} s_{k-1}^T, \tag{3.10}$$

where $H_{k,0}^{-1}$ denotes the initial guess of H_k^{-1}. In general, an effective choice of $H_{k,0}^{-1}$ is

$$H_{k,0}^{-1} = \frac{s_{k-1}^T y_{k-1}}{y_{k-1}^T y_{k-1}} I. \tag{3.11}$$

Then the search direction of L-BFGS recursive scheme can be summarized as the following steps

---

Search direction r_k: r_k=Direction($\partial E_k, \{s_i, y_i, k - n \leq i \leq k - 1\}$).

$\quad g = \partial E_k;$

$\quad$ For $\ i = k - 1, \cdots, k - n$

$\quad\quad g = g - \lambda_i y_i;$

$\quad$ End

$\quad q = H_{k,0}^{-1} g;$

$\quad$ For $\ i = k - n, \cdots, k - 1$

$\quad\quad q = q + s_i(\lambda_i - \rho_i y_i^T q);$

$\quad$ End

$\quad r_k = -q.$

3.3. Simple Bound Constraints

To enforce the physical nonnegativity or apply some lower and upper limits, simple bound of X is added as the constraint condition in the least-square model (3.1), i.e., the following reconstruction model

$$X = \arg\min_X \frac{1}{2}||p(X) - Y||^2, \quad s.t. \ L \leq X \leq U. \tag{3.12}$$

Then the aforesaid L-BFGS can be modified accordingly for solving this bound-constrained problem (3.12). Actually, only little modification to the search direction r is needed. Let

$$\hat{r}(X) = \text{Proj}(r) = \begin{cases} -L, & \text{if } X + r \leq L, \\ r, & \text{if } L < X + r < U, \\ -U, & \text{if } X + r \geq U. \end{cases} \tag{3.13}$$

Then from the well-known KKT conditions [26], it can be proved that $\hat{r}$ will be also a decent direction whenever r is a decent direction. Consequently, only one thing we need to do is to project direction r to $\hat{r}$ during the L-BFGS iterations.

As for the step size, the following modified Wolfe conditions can be used [26]

$$E(X_k + \lambda_k \hat{r}_k) \leq E(X) + \delta_1 \lambda_k \partial E^T(X_k)\hat{r}_k, \tag{3.14a}$$

$$\partial E^T(X_k + \lambda_k \hat{r}_k)\hat{r}_k \geq \delta_2 \partial E^T(X_k)\hat{r}_k, \tag{3.14b}$$

$$L \leq X_k + \lambda_k \hat{r}_k \leq U. \tag{3.14c}$$

In this work, the following backtracking line search scheme for updating step size λ_k is utilized.

Bound-constrained step size: $(\lambda, n) = \text{Backtrack}(\hat{r})$.
  Parameters: $\delta_1 = 0.0001, \delta_2 = 0.9, \rho = 0.25, n_{max} = 5$;
  Initialization: $\lambda_0 = 1, n = 1$;
  Do $\lambda_n = \rho\lambda_{n-1}$
    $n = n + 1$
  Until λ_n satisfies (3.14a) or $n = n_{max}$.

Our observation is that L-BFGS (3.10) with five truncation is generally sufficient. To summarize, the L-BFGS method for solving our bound-constrained limited-view MS-QPAT (3.12) is as the following:

Bound-constrained L-BFGS: $X_k = \text{Constrained-LBFGS}(X_0)$.
  Parameters: $M_{max} = 5, K_{max} = 200, \varepsilon = 0.001, k = 0, m = 0, n_{max} = 200$
  While $k \leq K_{max}, l \leq M_{max}, ||\partial E_k||_2/N \leq \varepsilon$
    $r_k = \text{Direction}(\partial E_k, \{s_i, y_i, k - l \leq i \leq k - 1\})$;
    $\hat{r_k} = \text{Proj}(r)$;
    $(\lambda_k, n_k) = \text{Backtrack}(\hat{r_k})$;
    $k = k + 1$;
    If $n_k == n_{max}$
      $l = l + 1$;
    End
  End

Here the number of inner iterations n_k is for updating λ_k and K_{max} means the maximum iterations of L-BFGS method.

In addition, since E_{ij} may change significantly, in order to balance the inhomogeneous discrepancy between the data and the model, the following weighted fidelity function is considered

$$E(X) = \frac{1}{2} \sum_{i=1}^{N_s} \sum_{j \in \mathcal{I}_i} \left(\frac{E_{ij}}{Y_{ij}} \right)^2. \tag{3.15}$$

Note that the weighting is used whenever $Y_{ij} \neq 0$ and if $Y_{ij} = 0$, it is truncated from (3.15) .

4. Sparsity Regularization

4.1. Sparsity-Regularized QPAT

In recent years, in order to overcome the ill-posedness of the problems and reduce the noise brought by imaging devices or system defects, a sparse regularization term is often added to improve the imaging quality motivated by the assumption that images can be well approximated by sparse coefficients under some transforms or designed systems. This kind of sparse regularization method has been proved to be effective and has been applied in almost every branch of imaging fields. In this MS-QPAT work, we consider the following sparsity-based optimization

$$\min_X \frac{1}{2} \| p(X) - Y \|_2^2 + \lambda \| WX \|_1, \text{ s. t. } L \leq X \leq U, \tag{4.1}$$

or the following sparsity-based constraint minimization problem with both data fidelity constraint and bound constraint of X

$$\min_X \| WX \|_1, \text{ s. t. } p(X) = Y, \quad L \leq X \leq U, \tag{4.2}$$

The bound constraint L and U on X has proved to be effective in our MS-QPAT experiments and moreover it can also accelerate the convergence of the corresponding Quasi-Newton algorithm used in solving the sub-problem. Here W denotes a sparse regularization operator. In recent years, various sparse transform operators or systems are designed, e.g., the first-order difference operator (total variation (TV)) [30] and wavelet based regularization operators are most widely used. These sparse operators have been particularly used in MS-QPAT, see [5, 17, 19, 32] for details. In this work, we use the tensor framelet (TF) transform [15, 18, 39] in our limited-view MS-QPAT reconstruction scheme, as a natural generalization of isotropic TV regularization to high orders.

4.1.1. Tensor Framelet

Compared with the traditional wavelet framelet, tensor framelet was introduced into image reconstruction for further improve the computing speed and memory. It can be regarded as a variant of standard wavelet tight frame [47] or a generalization of the isotropic gradient diffusion to high-order gradients. Tensor framelet has been applied to computed tomography [13, 15, 18, 38] and QPAT [37] etc. We start from the description of the traditional one-level 1D wavelet tight frame. More details are available in [15, 18].

Traditional wavelet tight frames can be constructed based on the Unitary Extension Principle (UEP) [45, 46], which are derived from a families of filters $h = \{h_i\}_0^{r-1}$ that make the associated analysis operator $W(h)$ and synthesis operator $W^T(h)$ satisfy $W^T W = I$.

Let $x \in R^N$ denote a given 1D signal. Then x is assumed sparse under the following so-called analysis operator denoted by $W(h)$

$$Wx = \left[\begin{array}{cccc} h_0 * x, h_1 * x, \cdots, h_{r-1} * x \end{array}\right]^T, \tag{4.3}$$

where $*$ denote the convolution operation.

Once the wavelet tight frame for 1D signal is constructed, the higher-dimensional wavelet tight frame for 2D images can be obtained via the vector tensor product denoted by $H = \{h_i \otimes h_j\}_0^{(r^2-1)}$. Then 2D images will accordingly be approximated by 2D wavelet tight frame associated with 2D convolution. Given a 2D image $X = \{X_{i,j}\} \in R^{MN}$, we have

$$WX = \left[\begin{array}{cccc} H_0 * X, H_1 * X, \cdots, H_{r^2-1} * X \end{array}\right]^T. \tag{4.4}$$

Here $*$ is used to also denote the corresponding 2D convolution operation.

Compared with the 1D convolution operation, 2D convolution means more memory and higher computational complexity. Therefore, instead of 2D convolution, tensor framelet (TF) for 2D image reconstruction is designed for improve the computational efficiency. This kind of tensor framelet is constructed from two families of 1D wavelet filters, and also satisfies the so-called perfect reconstruction property, i.e., $W^T W = I$.

Concretely, given a family of 1D filters $h^x = \{h_i^x\}_0^{r-1}$. Define

$$W_x(h^x): \ X \in R^{MN} \rightarrow \left[\begin{array}{c} h_0^x *_x X \\ \vdots \\ h_{r-1}^x *_x X \end{array}\right] \in R^{rMN}. \tag{4.5}$$

Here $*_x$ denote the filtering along x direction with 1D filters h^x, i.e., filtering column-wisely. Similarly, given another family of 1D filters $h^y = \{h_i^y\}_0^{r-1}$,

$$W_y(h^y): \ X \in R^{MN} \rightarrow \left[\begin{array}{c} h_0^y *_y X \\ \vdots \\ h_{r-1}^y *_y X \end{array}\right] \in R^{rMN}, \tag{4.6}$$

where $*_y$ is the filtering along y direction with 1D filters h^y, i.e., filtering row-wisely. Then the constructed 2D tensor framelet for 2D images associated with two families of filters h^x and h^y is defined as

$$W(h^x, h^y): X \in R^{MN} \rightarrow \frac{1}{\sqrt{2}} \left[\begin{array}{c} W_x(h^x)X \\ W_y(h^y)X \end{array}\right] \in R^{2rMN}. \tag{4.7}$$

If h^x and h^y satisfy the UEP condition, then $W_x(h^x)^T W_x(h^x) = I$, $W_y(h^y)^T W_y(h^y) = I$, and

$$W(h^x, h^y)^T W(h^x, h^y) = \frac{1}{2}(W_x(h^x)^T W_x(h^x) + W_y(h^y)^T W_y(h^y)) = I.$$

The 2D tensor framelet operator $W_T(h^x, h^y)$ is therefore a tight frame in this circumstance.

Define

$$H_m X|_{ij} = \left(\begin{array}{c} H_{mx} X|_{ij} \\ H_{my} X|_{ij} \end{array}\right) = \left(\begin{array}{c} h_m^x *_x X|_{ij} \\ h_m^y *_y X|_{ij} \end{array}\right), \quad m = 0, 1, \cdots, r-1. \tag{4.8}$$

Then the TF norm can be defined as

$$||W_T X||_1 = w_0||H_0 X||_1 + w_1||H_1 X||_1 + \cdots + w_{r-1}||H_{r-1} X||_1, \tag{4.9}$$

where $\{w_i\}_0^{r-1}$ are the corresponding weights of the following norms

$$||H_m X||_1 = \sum_{ij} \sqrt{(H_{mx} X|_{ij})^2 + (H_{my} X|_{ij})^2}, \quad m = 0, 1, \cdots, r-1. \tag{4.10}$$

A widely used wavelet tight frame is the linear B-spline framelet whose associated filters are

$$h_0 = \frac{1}{4}[1,2,1], \quad h_1 = \frac{\sqrt{2}}{4}[1,0,-1], \quad h_2 = \frac{1}{4}[-1,2,-1]. \tag{4.11}$$

This linear framelet has been applied in many image processing tasks [44]. In this work, the tensor framelet means the filters $h^x = \{h_i^x\}_0^{r-1}$ and $h^y = \{h_i^y\}_0^{r-1}$ are both chosen to be the linear B-Spline filters (4.11),i.e.,

$$H_0 X|_{ij} = \begin{pmatrix} H_{0x}X|_{ij} \\ H_{0y}X|_{ij} \end{pmatrix} = \frac{1}{4\sqrt{2}} \begin{pmatrix} X_{i+1,j} + 2X_{ij} + X_{i-1,j} \\ X_{i,j+1} + 2X_{ij} + X_{i,j-1} \end{pmatrix}, \tag{4.12}$$

$$H_1 X|_{ij} = \begin{pmatrix} H_{1x}X|_{ij} \\ H_{1y}X|_{ij} \end{pmatrix} = \frac{1}{4} \begin{pmatrix} X_{i+1,j} - X_{i-1,j} \\ X_{i,j+1} - X_{i,j-1} \end{pmatrix}, \tag{4.13}$$

$$H_2 X|_{ij} = \begin{pmatrix} H_{2x}X|_{ij} \\ H_{2y}X|_{ij} \end{pmatrix} = \frac{1}{4\sqrt{2}} \begin{pmatrix} -X_{i+1,j} + 2X_{ij} - X_{i-1,j} \\ -X_{i,j+1} + 2X_{ij} - X_{i,j-1} \end{pmatrix}. \tag{4.14}$$

The corresponding TF norm will be

$$||W_T X||_1 = w_0||H_0 X||_1 + w_1||H_1 X||_1 + w_2||H_2 X||_1, \tag{4.15}$$

where

$$||H_m X||_1 = \sum_{ij} \sqrt{(H_{mx}X|_{ij})^2 + (H_{my}X|_{ij})^2}, \quad m = 0,1,2. \tag{4.16}$$

Higher-dimensional tensor framelet at multi-level can be seen in [15,18].

Specially, if two filters $h^x = h^y = [1,-1]$ are used in convolution, then (4.15) is exactly the TV regularization and (4.16) is the so-called isotropic TV norm. Consequently tensor framelet we constructed in this work can be regarded as a variant of traditional wavelet tight framelet and also can be treated as a generalization of isotropic TV.

4.2. Optimization Algorithm

We restate the sparsity-regularized MS-QPAT reconstruction problem

$$\min_X ||W_T X||_1, \quad \text{s.t.} \quad p(X) = Y, \ L \leq X \leq U. \tag{4.17}$$

Here W_T is the aforementioned tensor framelet based on B-Spline linear filters. Here we only provide the algorithm for (4.17) (small-noise case), and the algorithm for (4.1) (large-noise case) is similar.

Observe that (4.17) is a nonlinear and nonconvex problem and the L1 regularization term is non-differentiable. In [37], forward-backward splitting algorithm is developed to handle the nonconvex MS-QPAT reconstruction problem with established convergence analysis. In this work, we develop the reconstruction algorithm based on alternating direction method of multipliers (ADMM) [8] or so-called split Bregman method [23], which is often used in solving the L1 non-differentiable problem. With ADMM algorithm the nonconvex and nonlinear function p can be solved by using Quasi-Newton method as the inner loop.

Let $C = \{K \in R^{MN} : L \leq K \leq U\}$. Define the indicator function of C as

$$\gamma_C(K) = \begin{cases} 0, & \text{if} \ K \in C, \\ +\infty, & \text{otherwise.} \end{cases} \tag{4.18}$$

Then by introducing another variable Z to overcome the non-differential property, problem (4.17) can be rewritten as

$$\min_X ||Z||_1 + \gamma_C(K), \text{ s. t. } p(X) = Y, \ W_T X = Z, \ X = K. \tag{4.19}$$

Then the ADMM iteration method for solving the limited-view MS-QPAT problem (4.17) can be formulated as the following decoupled equations:

$$\begin{cases} X^{n+1} = \arg\min_X \frac{\alpha}{2}||p(X) - Y + b_1||_2^2 + \frac{\beta}{2}||W_T X - Z + b_2||_2^2 + \frac{\gamma}{2}||X - K + b_3||_2^2, \\ Z^{n+1} = \arg\min_Z ||Z||_1 + \frac{\beta}{2}||WX - Z + b_2||_2^2, \\ K^{n+1} = \arg\min_K \gamma_C(K) + \frac{\beta}{2}||X - K + b_3||_2^2, \\ b_1^{n+1} = p(X) - Y + b_1, \\ b_2^{n+1} = W_T X - Z + b_2, \\ b_3^{n+1} = X - K + b_3. \end{cases} \tag{4.20}$$

As for the X sub-problem, we can use the unconstrained L-BFGS method mentioned above, for which only the gradient is slightly different. Let

$$E(X) = \frac{\alpha}{2}||p(X) - Y + b_1||_2^2 + \frac{\beta}{2}||W_T X - Z + b_2||_2^2 + \frac{\gamma}{2}||X - K + b_3||_2^2.$$

The numerical gradient of $E(X)$ is

$$\frac{\partial E}{\partial X} = \alpha(p - Y + b_1)\frac{\partial p}{\partial X} + \beta W_T^T\Big(W_T X - (Z - b_2)\Big) + \gamma(X - K + b_3). \tag{4.21}$$

So the adjoint acoustic source is modified accordingly in the solver (3.3),

$$Q_a^i = \alpha \sum_{j \in \mathcal{J}_i} (p_{ij} - Y_{ij} + b_{1,ij})M_j. \tag{4.22}$$

Then the numerical gradient can be obtained by adding $\beta W_T^T(W_T X - (Z - b_2)) + \gamma(X - K + b_3)$ to the adjoint method (3.5).

As for the Z sub-problem, generalized shrinkage formula can be used to solve this problem. Let

$$s_{mx}|_{ij} = H_{mx}X|_{ij} + b_{2m}^x|_{ij},$$
$$s_{my}|_{ij} = H_{my}X|_{ij} + b_{2m}^y|_{ij}.$$

Since

$$Z^{n+1} = \arg\min_Z \sum_{m=0}^{2} \sum_{ij} \left\{ \frac{\beta}{2}[Z_{ij}^{x,m} - (s_{mx}|_{ij})]^2 + \frac{\beta}{2}[Z_{ij}^{y,m} - (s_{my}|_{ij})]^2 \right.$$
$$\left. + \sqrt{(Z_{ij}^{x,m})^2 + (Z_{ij}^{x,m})^2} \right\},$$

Then the generalized shrinkage formula denoted by S_β can be solved as follows

$$Z_{ij}^{x,m} = \max\left(\sqrt{(s_{mx}|_{ij})^2 + (s_{my}|_{ij})^2} - \frac{1}{\beta}, 0\right) \frac{(s_{mx}|_{ij}, s_{my}|_{ij})}{\sqrt{(s_{mx}|_{ij})^2 + (s_{my}|_{ij})^2}}. \tag{4.23}$$

As for the K sub-problem, the following well-known proximity operator $\text{prox}_\varphi : H \to H$ defined as

$$\text{prox}_\varphi(x) := \arg\min_y \left\{ \frac{1}{2}||x - y||_2^2 + \varphi(y) : y \in H \right\} \tag{4.24}$$

can be used. Then

$$\text{prox}_{\gamma_C}(x) = \begin{cases} x, & \text{if } x \in C, \\ U, & \text{if } x > U, \\ L, & \text{if } x < L. \end{cases} \tag{4.25}$$

Algorithm 4.1: ADMM for solving (4.19)

Choose: parameters λ, β, γ;

Initialization: b_1, b_2, b_3.

For $n = 1, \cdots, m$ $\quad X^{n+1} = X^n + \lambda_n r_n,$

$\quad r_{n+1} = \text{Direction}(\partial E(X^n)),$

$\quad \lambda_{n+1}$ is selected by Wolfe conditions,

$\quad Z^{n+1} = S_\beta(W_T X^{n+1} + b_2^n),$

$\quad K^{n+1} = \text{prox}_{\gamma_C}(X^{n+1} + b_3^n),$

$\quad b_1^{n+1} = b_1^n + p(X^{n+1}) - Y,$

$\quad b_2^{n+1} = b_2^n + W_T X^{n+1} - Z^{n+1},$

$\quad b_3^{n+1} = b_3^n + X^{n+1} - K^{n+1}.$

End

Another method we can solve X sub-problem is that we first solve the unconstrained problem, i.e.,

$$\min_X \frac{\alpha}{2}\|p(X) - Y + b_1\|_2^2 + \frac{\beta}{2}\|W_T X - Z + b_2\|_2^2$$

using the L-BFGS method and then consider $L < X < U$, i.e., the L-BFGS for bound-constrained $L < X < U$. We briefly write the constrained ADMM iteration algorithm as follows

---

Algorithm 4.2: ADMM based on L-BFGS method with bound-constraint for solving (4.19)

Choose: parameters λ, β;

Initialization: b_1, b_2.

For $n = 1, \cdots, m$

$\quad X^{n+1} = \text{Constrained-LBFGS}(X^n, Z^n, b_1^n, b_2^n),$

$\quad Z^{n+1} = S_\beta(W_T X^{n+1} + b_2^n),$

$\quad b_1^{n+1} = b_1^n + p(X^{n+1}) - Y,$

$\quad b_2^{n+1} = b_2^n + W_T X^{n+1} - Z^{n+1}.$

End

The modified L-BFGS method with simple bound constraint, i.e., Algorithm 4.2 can slightly speed up the numerical solution compared with Algorithm 4.1 based on numerical simulations. In the following, we use Algorithm 4.2 for simulation.

5. Results

This section presents the simulation results to validate the proposed method. For the limited-view scanning with four optical illuminations, the ultrasonic transducers are designed
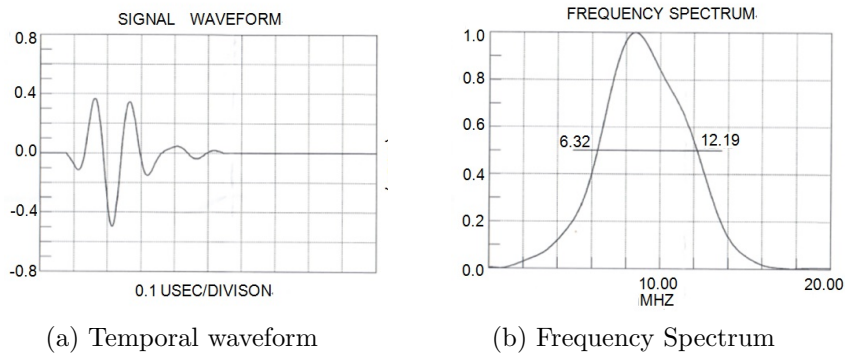
(a) Temporal waveform   (b) Frequency Spectrum

Fig. 5.1. Experimental EIR. (a) The temporal waveform of experimental EIR with temporal duration 0.3μs. (b) The spectrum of experimental EIR with central frequency 8.51MHz, and pass-band frequency [6.32, 12.19MHz].
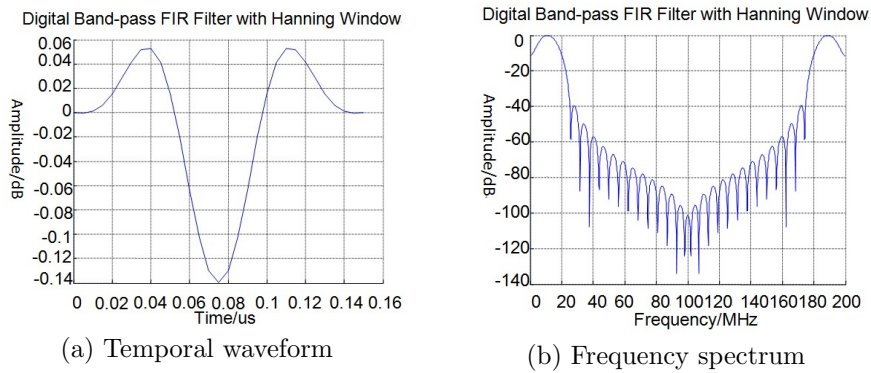

(a) Temporal waveform   (b) Frequency spectrum

Fig. 5.2. Simulated FIR filter.

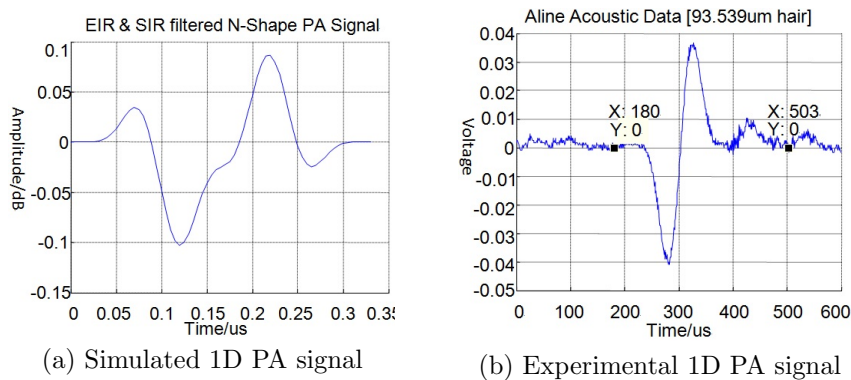(a) Simulated 1D PA signal   (b) Experimental 1D PA signal

Fig. 5.3. One-dimensional PA data estimation.

to rotate 90° together with the illuminations with the total data acquisition completed in one rotation, so that the acoustic data are collected only near the illumination sources for improved SNR and reduced scanning time.

The temporal waveform and the frequency spectrum of experimental EIR are listed in Fig. 5.1. The corresponding test conditions are as follows. Transducer type: No. Olympus NDT V311-SU; standard central frequency of transducer: 10MHz; pulser setting: energy 100 Volt,

(a) Ground truth

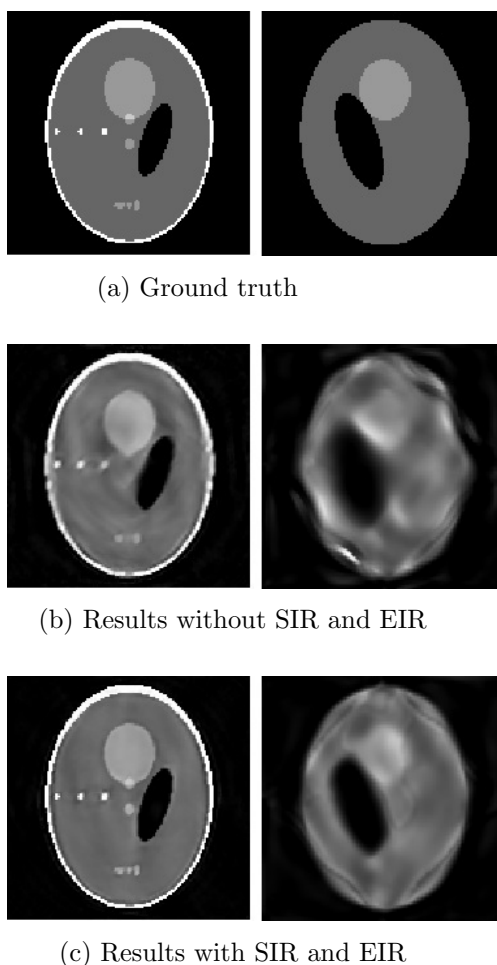(b) Results without SIR and EIR

(c) Results with SIR and EIR

Fig. 5.4. Reconstruction results with initial guesses $\mu_a = 0.012$, $\mu'_s = 1.2$. Images in (a) (from left to right) are respectively the ground truth of μ_a and μ'_s; Images in (b) (from left to right) are respectively the reconstructed μ_a and μ'_s without SIR and EIR; Images in (c) (from left to right) are the reconstructed μ_a and μ'_s by our proposed method with SIR and EIR.

damping 50 Ohm, spike shape; receiver setting: gain 23dB, filter 2.0-21.5MHz; target: 2 inch silica. In this study, EIR can be approximated by a finite-impulse-response (FIR) digital filter (Fig. 5.2) through a window function method. The pass-band frequency is set as [8, 12.5MHz] with a central frequency as 10MHz. Given that the simulated sampling frequency might reach at 100MHz for data acquisition in forward modeling, the temporal duration of FIR filter is set to be $0.3\mu s$ (30 points in discrete domain) according to the database of transducer itself. The simulated 1D PA signal and the experimental 1D PA signal of a hair thread with $93\mu m$ in diameter are illustrated in Fig. 5.3, which demonstrates the advantages of incorporating the SIR and EIR.

As for the two-dimensional circumstance, the limited MS-QPAT scheme is simulated on a Shepp-Logan phantom (Fig. 5.4). Images in Fig. 5.4(a) (from left to right) are respectively the ground truth of absorption coefficient μ_a and scattering coefficient μ'_s; four illuminations

are located equally at the boundary of the image square domain. The values of the parameters used in the numerical experiment are as follows: $g = 0, \kappa = 2.74, c = 1.5, C_p = \beta = 1, \varepsilon = 40/128 = 0.3125$, and g is the delta function. Both the absorption and the scattering maps are reconstructed simultaneously by using the proposed scheme. The reconstruction of scattering coefficient is more ill-posed using the DA forward model. The displayed 128×128 images have the same display windows, i.e., [0.01 0.02] for μ_a and [1 2] for μ'_s, and the simulation data has one percent Gaussian noise. From Fig. 5.4(c), we can see that the proposed method with SIR and EIR could completely reconstruct the absorption coefficient μ_a and meanwhile improve the reconstructed results compared with the method without SIR and EIR (Fig. 5.4(b)).

6. Conclusion

This paper has considered a practical image reconstruction scheme for multi-source QPAT. The spatial impulse response (SIR) and acousto-electric impulse (EIR) response are incorporated to accurately model the QPAT measurement and the limited-view scheme is used to take the measurement near optical sources to reduce the data acquisition time and meanwhile improve the SNR. A coupled opto-acoustic image reconstruction algorithm that incorporates SIR, EIR and limited-view scanning is proposed, and solved by alternating direction method of multipliers with tensor framelet regularization. Simulated experimental results demonstrate that the proposed method with SIR and EIR improves the reconstructed image quality from that without SIR and EIR.

References

[1] K. Feng, Differential vs. integral equations and finite vs. infinite elements, *Math. Numer. Sinica.*, **2** (1980), 100-105.

[2] S.R. Arridge, Optical tomography in medical imaging, *Inverse Probl.*, **15** (1999), 41-93.

[3] Q. Sheng, K. Wang, T.P. Matthews, J. Xia, L. Zhu, L.V. Wang and M.A. Anastasio, A Constrained Variable Projection Reconstruction Method for Photoacoustic Computed Tomography Without Accurate Knowledge of Transducer Responses, *IEEE. Trans. med. Imag.*, **34**(2015), 2443-2458.

[4] M. Xu and L.V. Wang, Analytic explanation of spatial resolution related to bandwidth and detector aperture size in thermoacoustic or photoacoustic reconstruction, *Phys. Rev. E. Stat. Nonlin. Soft Matter Phys.*, **67** (2003), 056605.

[5] G. Bal and K. Ren, Multi-source quantitative photoacoustic tomography in a diffusive regime, *Inverse Probl.*, **27** (2011), 075003.

[6] G. Bal and K. Ren, On multi-spectral quantitative photoacoustic tomography in diffusive regime *Inverse Probl.*, **278** (2012), 025010.

[7] P.C. Beard, Biomedical photoacoustic imaging, *Interface Focus*, **1** (2011), 602-631.

[8] E. Esser, Applications of Lagrangian-based alternating direction methods and connections to split Bregman, Univ. California, Los An-geles, *Computat. Appl. Math. Tech. Rep.*, (2009), 09-31.

[9] R.H. Byrd, J. Nocedal and R.B. Schnabel, Representations of quasi-Newton matrices and their use in limited-memory methods, *Mathematical Programming, Series A*, **63** (1994), 129-156.

[10] B.T. Cox, S.R. Arridge, and P.C. Beard, Estimating chromophore distributions from multiwave-length photoacoustic images, *J. Opt. Soc. Am. A.*, **26** (2009), 443-455.

[11] K. Wang, S.A. Ermilov, R. Su, H. Brecht, A.A. Oraevsky, and M.A. Anastasio, An imaging model incorporating ultrasonic transducer properties for three-dimensional optoacoustic tomography, *IEEE. Trans. Med. Imag.*, **30** (2011), 203-214.

[12] B.T. Cox, J.G. Laufer, S.R. Arridge and P.C. Beard, Quantitative spectroscopic photoacoustic imaging: a review, *J. Biomed. Opt.*, **17** (2012), 061202.

[13] H. Ding, H. Gao, B. Zhao, H-M. Cho and S. Molloi, A high-resolution photon-counting breast CT system with tensor-framelet based iterative image reconstruction for radiation dose reduction, *Phys. Med. Biol.*, **59** (2014), 6005.

[14] S.A. Ermilov, T. Khamapirad, A. Conjusteau, M.H. Leonard, R. Lacewell, K. Mehta, T. Miller and A.A. Oraevsky, Laser optoacoustic imaging system for detection of breast cancer, *J. Biomed. Opt.*, **14** (2009), 024007.

[15] H. Gao, R. Li, Y. Lin and L. Xing, 4D cone beam CT via spatiotemporal tensor framelet, *Med. Phys.*, **39** (2012), 6943-6946.

[16] H. Gao and H. Zhao, A fast forward solver of radiative transfer equation, *Transport. Theor. Stat.*, **38** (2009), 149-192.

[17] H. Gao, H. Zhao and S. Osher, Bergman methods in quantitative photoacoustic tomography, *UCLA CAM Report*, (2010), 10-24.

[18] H. Gao, X.S. Qi, Y. Gao and D.A. Low, Megavoltage CT imaging quality improvement on To-moTherapy via tensor framelet, *Med. Phys.*, **40** (2013), 081919.

[19] H. Gao, S. Osher, and H. Zhao, Quantitative photoacoustic Tomography, *Mathematical Modeling in Biomedical Imaging II: Lecture Notes in Mathematics*, (2012), 131-158.

[20] H. Gao, L. Phan and Y. Lin, Parallel multigrid solver of radiative transfer equation for photon transport via graphics processing unit, *J. Biomed. Opt.,* **17** (2012), 096004.

[21] H. Gao and H. Zhao, Multilevel bioluminescence tomography based on radiative transfer equation Part 1: l1 regularization,*Opt. Express.*, **18** (2010), 1854-1871.

[22] H. Gao and H. Zhao, Multilevel bioluminescence tomography based on radiative transfer equation Part 2: total variation and l1 data fidelity, *Opt. Express.*, **18** (2010), 2894-2912.

[23] T. Goldstein and S. Osher, The split Bregman algorithm for l1 regularized problems,*SIAM J. Imaging Sci.*, **2** (2009), 323-343.

[24] R.A. Kruger, P. Liu and C.R. Appledorn, Photoacoustic ultrasound (PAUS) reconstruction to-mography, *Med. Phys.*, **22** (1995), 1605-1609.

[25] A.V. Mamonov and K. Ren, Quantitative photoacoustic imaging in radiative transport regime, *Commun. Math. Sci.*, **12** (2014), 201-234.

[26] J. Nocedal and S.J. Wright, Numerical Optimization, Springer, New York, 2006.

[27] D. Razansky, M. Distel, C. Vinegoni, R. Ma, N. Perrimon, R.W. Köster and V. Ntziachristos, Mul-tispectral opto-acoustic tomography of deep-seated fluorescent proteins in vivo, *Nat. Photonics.*, **3** (2009), 412-417.

[28] A.B. Pulkkinen, T. Cox, S.R. Arridge, J.P. Kaipio and T. Tarvainen, A Bayesian approach to spectral quantitative photoacoustic tomography, *Inverse Probl.*, **30** (2014), 065012.

[29] K. Ren, H. Gao and H. Zhao, A hybrid reconstruction method for quantitative PAT, *SIAM J. Imaging Sci.,* **6** (2013), 32-55.

[30] L. Rudin, S. Osher, and E. Fatemi, Nonlinear total variation based noise removal algorithms, *J. Phys. D.*, **60** (1992), 259-268.

[31] P. Shao, B.T. Cox, and R.J. Zemp,. Estimating optical absorption scattering and Grueneisen distributions with multiple-illumination photoacoustic tomography, *Appl. Opt.*, **50** (2011), 3145-3154.

[32] T. Tarvainen, B.T. Cox, J.P. Kaipio and S.R. Arridge, Reconstructing absorption and scattering distributions in quantitative photoacoustic tomography, *Inverse Probl.*, **28** (2012), 084009.

[33] L.V. Wang, Multiscale photoacoustic microscopy and computed tomography, *Nat. Photonics.*, **3** (2009), 503-509.

[34] L.V. Wang and S. Hu, Photoacoustic tomography: in vivo imaging from organelles to organs, *Science*, **335** (2012), 1458-1462.

[35] M. Xu and L.V. Wang, Photoacoustic imaging in biomedicine, *Rev. Sci. Instrum.*, **77** (2006), 041101.

[36] Y. Xu, L.V. Wang, Ambartsoumian G, and Kuchment P, Reconstructions in limited-view thermoacoustic tomography, *Med. Phys.*, **31** (2004), 724-733.

[37] X. Zhang, W. Zhou, X. Zhang and H. Gao, Forward-backward splitting method for quantitative photoacoustic tomography, *Inverse Probl.*, **30** (2014), 125012.

[38] B. Zhao, H. Gao, H. Ding, and S. Molloi, Tight-frame based iterative image reconstruction for spectral breast CT, *Med. Phys.*, **40** (2013), 031905.

[39] W. Zhou, J-F Cai and H. Gao, Adaptive tight frame based medical image reconstruction: a proof-of-concept study for computed tomography, *Inverse Probl.*, **29** (2013), 125006.

[40] L.V. Wang, Photoacoustic Imaging and Spectroscopy, CRC Press, Boca Raton, 2009.

[41] S.A. Ermilov, M.P. Fronheiser, H.-P. Brecht, R. Su, A. Conjusteau, K. Mehta, P.Otto, and A.A. Oraevsky, Development of laser optoacoustic and ultrasonic imaging system for breast cancer utilizing handheld array probes, *Proc. SPIE.*, **7177** (2009), 717703-717710.

[42] A. Conjusteau, S.A. Ermilov, R. Su, H.P. Brecht, M.P. Fronheiser and A.A. Oraevsky, Measurement of the spectral directivity of optoacoustic and ultrasonic transducers with a laser ultrasonic source, *Rev. Sci. Instrum.*, **80** (2009).

[43] H. Gao, J. Feng and S. Liang, Limited-view multi-source quantitative photoacoustic tomography, *Inverse Probl.*, **31** (2015), 065004.

[44] J-F. Cai, B. Dong, S. Osher and Z. Shen, Image restorations: total variation, wavelet frames and beyond, *J. Amer. Math. Soc.*, **25** (2012), 1033-1089.

[45] A. Ron and Z. Shen, Affine systems in $L^2(R^d)$: The analysis of the analysis operator. *J. Func. Anal.*, **148** (1997), 408-447.

[46] I. Daubechies, B. Han, A. Ron and Z. Shen, Framelets: MRA-based constructions of wavelet frames, *Appl. comput. harmon. anal.*, **14** (2003), 1-46.

[47] B. Dong and Z. Shen, MRA based wavelet frames and applications, IAS Lecture Notes Series, Summer Program on The Mathematics of Image Processing? Park City Mathematics Institute, 2010.